

Multi-messenger emission from magnetic reconnection in blazar jets: the case of TXS 0506+056

E. M. de Gouveia Dal Pino^{1,*}, J. C. Rodríguez-Ramírez^{1,2}, M. V. del Valle¹

¹ Instituto de Astronomia, Geofísica e Ciências Atmosféricas Universidade de São Paulo IAG, Rua do Matão 1225, CEP: 05508-090 São Paulo - SP - Brazil.

² Centro Brasileiro de Pesquisas Físicas, Rua Dr. Xavier Sigaud, 150, CEP: 22290-180, Rio de Janeiro - RJ - Brazil.

Accepted XXX. Received YYY; in original form ZZZ

ABSTRACT

Measurements from astroparticle experiments, such as the 2017 flare associated with the source TXS 0506+056, indicate that blazars act as multi-messenger (MM; radiation and neutrinos) factories. Theoretically, the particle acceleration mechanisms responsible for blazar emissions and the precise location within the jet where this occurs remain undetermined. This paper explores MM emission driven by magnetic reconnection in a blazar jet. Previous studies have shown that reconnection in the magnetically dominated regions of these relativistic jets can efficiently accelerate particles to very high energies (VHE). Assuming that turbulent-driven magnetic reconnection accelerates cosmic-ray protons and electrons by a Fermi process, we developed a lepto-hadronic radiation model without the influence of external soft-photons to explain the 2017 MM flare from TXS 0506+056. In the proposed scenario, the emission blob moves downstream in the jet from ~ 2 to 4 pc from the central engine, which is a supermassive black hole (SMBH) of $3 \times 10^8 M_{\odot}$ launching a jet with $150L_{\text{Edd}}$ power. As the blob moves, we observe a sequence of spectral energy distribution (SED) profiles that match the observed arrival of the high energy neutrino and electromagnetic emission from TXS 0506+056. This arrival coincides with the high state of intermediate energy γ -rays ($E \sim 1$ GeV) detection, followed by the subsequent appearance of the VHE γ -ray signal and then no further significant neutrino detection. We obtain a time delay between the neutrino and VHE events ≈ 6.4 days, which is consistent with that observed in the 2017 MM flare.

Key words: AGN blazars – magnetic reconnection – radiation: non-thermal

1 INTRODUCTION

Relativistic jets are collimated outflows of plasma propagating at relativistic speeds, commonly observed in active galaxies and, on a much smaller scale, in our own galaxy in sources known as microquasars. These high-energy outflows are generated and energized by supermassive black holes (SMBHs) and stellar-mass black holes, respectively. Even more extreme cases occur in gamma-ray bursts, which are powered by the collapse of compact stars into black holes (e.g. de Gouveia Dal Pino et al. 2020, and references therein). One of the most accepted explanations for the origin of such energetic collimated outflows is the Blandford-Znajek mechanism (Blandford & Znajek 1977; McKinney et al. 2012). In this scenario, relativistic jets are launched by magnetic torques of accumulated field lines anchored to the highly spinning BHs. If this description is accurate, relativistic jets are expected to be born magnetically dominated and hence they must convert magnetic to kinetic energy to achieve their observed relativistic speeds and emissions (e.g. Giannios et al. 2009; Giannios 2010; de Gouveia Dal Pino et al. 2020, for reviews)

Functioning as highly efficient particle accelerators, these jets frequently emit radiation at GeV and TeV energies (see e.g. review by Hovatta & Lindfors 2019). Recent observations have provided

compelling evidence of these jets' ability to accelerate protons, as demonstrated by the case of TXS 0506+056, where simultaneous emissions of high-energy gamma-rays and neutrino were detected (IceCube Collaboration et al. 2018b). However, ongoing discussions within the scientific community raise questions regarding the extent to which these jets contribute to the observed astrophysical neutrinos (both diffuse and localized) recorded by instruments like IceCube (e.g. Khiali & de Gouveia Dal Pino 2016; IceCube Collaboration et al. 2018a,b; Plavin et al. 2020, 2021; Hovatta et al. 2021; Abbasi et al. 2022; Buson et al. 2022; Bellenghi et al. 2023),

Recently, in light of ongoing debates on the origin of cosmic ray (CR) acceleration and very high energy (VHE) variable emission, particularly in blazars (e.g. Aharonian et al. 2007; Ackermann et al. 2016; Britto et al. 2016; IceCube Collaboration et al. 2018a,b), extensive studies have been conducted on particle acceleration by magnetic reconnection in magnetically dominated regions where shocks are faint or absent. Our understanding of particle acceleration driven by magnetic reconnection has significantly advanced due to both particle-in-cell (PIC) simulations predominantly performed in two-dimensions (2D) (e.g. Lyubarsky & Liverts 2008; Li et al. 2015; Petropoulou et al. 2016; Werner et al. 2019; Lyutikov et al. 2017; Sironi & Spitkovsky 2014; Guo et al. 2020; Kilian et al. 2020; Comisso & Sironi 2018; Cerruti 2020; Guo et al. 2022), and 3D magnetohydrodynamic (MHD) simulations (e.g. Kowal et al. 2011,

* E-mail: dalpino@iag.usp.br, juancr@cbpf.br

2012; de Gouveia Dal Pino & Kowal 2015; del Valle et al. 2016; Beresnyak & Li 2016; Ripperda et al. 2017; Kadowaki et al. 2021; Medina-Torrejón et al. 2021; Zhang et al. 2023a; Medina-Torrejón et al. 2023). While PIC simulations probe the micro-scales of the process, studying acceleration up to at most 10^4 times the particle's rest mass, MHD simulations with test particles probe the macro-scales, detecting particle acceleration up to observed VHE and ultra-high energies (UHECRs) (Medina-Torrejón et al. 2021, 2023).

In particular, Medina-Torrejón et al. (2021), Kadowaki et al. (2021), and Medina-Torrejón et al. (2023), conducted 3D MHD and 3D MHD-PIC simulations exploring how relativistic jets transition from magnetically to kinetically dominated states with a magnetization parameter (given by the ratio between the magnetic and the rest mass energy density) close to 1. They observed that jets, affected by current-driven kink instability become turbulent, forming multiple fast reconnection layers at all scales of the turbulent flow (as predicted by Lazarian & Vishniac 1999, theory). Test protons injected into this turbulent flow with reconnection layers undergo acceleration with nearly exponential energy growth in time, primarily in their parallel momentum component, akin to a Fermi process (de Gouveia Dal Pino & Lazarian 2005). They reach threshold energies, with Larmor radius as large as the size of the jet diameter, before undergoing further, slower acceleration drifting in non-reconnecting magnetic fields. Other studies involving PIC simulations of relativistic jets subject to kink instability (Davelaar et al. 2020) and other driving mechanisms of turbulence such as Weibel, kinetic Kelvin-Helmholtz, and mushroom instability (Nishikawa et al. 2020), have also detected particle acceleration by magnetic reconnection, though to much smaller energies, as allowed by the small scales probed by kinetic (PIC) simulations. These findings underscore the potential of magnetic reconnection to drive particle acceleration, potentially explaining UHE phenomena in blazars (see also Giannios 2010; de Gouveia Dal Pino et al. 2020). Whether or not this process produces observable multi-messenger emissions can be tested, for the first time, using the 2017 multi-messenger flare from TXS 0506+056.

TXS 0506+056 is a well-known blazar localized at redshift $z = 0.34$ (Paiano et al. 2018). A high-energy neutrino event, a muon neutrino with $E \sim 290$ TeV (IceCube-170922A), detected by IceCube on 22 September 2017 was coincident in direction and time with a gamma-ray flare from this source (IceCube Collaboration et al. 2018b). Analysis of 9.5 years archival IceCube data revealed that this blazar was emitting neutrinos between October 2014 and March 2015. An excess of 13 ± 5 events above the expectation from the atmospheric background was found. In opposition to IceCube-170922A, no electromagnet flaring activity was present during these neutrino events (IceCube Collaboration et al. 2018a). Both occurrences prove blazars as the first identifiable sources of the high-energy astrophysical neutrino flux.

Under the hypothesis that the IC-170922A neutrino and the 2017 MW flaring state of TXS 0506+056 both originated in the blazar jet, multiple radiative approaches have been explored to explain the MM data. Considering the photo-pion reaction as the principal channel for neutrino production in the jet, independent studies appear to agree that mixed (also called hybrid) lepto-hadronic scenarios lead to higher rates of neutrinos production compared to proton synchrotron models at energies consistent with the IC-170922A event (Cerruti et al. 2019; Keivani et al. 2018; Gao et al. 2019). Regarding the source of target photons for photo-pion production, the simplest scenarios assume that the target photons are synchrotron photons from primary electrons within the jet, which are the same photons that produce the low-energy bump in the observed SED (Cerruti et al. 2019; Gao et al. 2019). Models assisted with external sources of radiation,

such as a putative broad line region (BLR) (Keivani et al. 2018; Xue et al. 2019), or an external sheath region of a structured jet (Ansoldi et al. 2018), can also in principle explain the MM SED. Although scenarios with external target photons add complexity to the radiation model (as it is not clear yet where the photons come from in TXS 0506+056), they have the characteristic of demanding less jet power compared to models with only internal soft photons. High-energy neutrinos can also be produced through the proton-proton (pp) hadronic channel. However, the rate of pp interactions in blazar jets is generally negligible compared to the rate of photo-pion production, unless external mechanisms are present. Under this line, the MM flare from TXS 0506+056 has also been investigated as a blazar jet interacting with an external obstacle (such as a BLR cloud or a star envelope Sahakyan 2018; Liu et al. 2019).

In this paper, we propose that the multi-messenger (MM) emission from the 2017 flare of TXS 0506+056 is driven by magnetic reconnection in the blazar jet. To explore the maximum possible neutrino production at energy levels consistent with the IC-170922A event, we adopt a hybrid lepto-hadronic model, assuming the absence of external sources of soft radiation for the simplest possible radiative scenario. In our model, we allow the large-scale properties of the blazar jet to transition from a magnetically dominated to a kinetically dominated flow as it propagates. We then derive MM emission at the jet locations where magnetic reconnection is likely the operating mechanism of particle acceleration. With this approach, as the emission region moves downstream with the jet flow, it produces a sequence of SEDs that are able to reproduce the 2017 MM flare from the blazar TXS-0506+056.

The paper is organised as follows. In section 2, we present the analytic model that we adopt to parametrise the macroscopic properties of the jet as a function of the distance from the central black hole. In Section 3, we describe the basic assumptions for deriving the MM emission from the jet. We apply this emission scenario, based on particle acceleration by magnetic reconnection within the emission region, to interpret the SED of the 2017 MM flare from the source TXS-0506+056 in Section 4. Finally, in Section 5 we summarise the present study and list our concluding remarks.

2 MAGNETIC DISSIPATION THROUGH THE JET FLOW

The numerical simulations involving particle acceleration by magnetic reconnection described above that were able to probe the production of very high energy cosmic rays have a very complex environment with a large scale helical magnetic field mixed with a turbulent component (e.g. Medina-Torrejón et al. 2021, 2023). In this background, particles are accelerated in the reconnection layers (or current sheets) driven by the turbulence. In order to build a similar but simpler scenario able to provide an analytical description of the development of fast reconnection and magnetic energy dissipation to energize particles and allow for MM emission, we here adopt a simpler picture, which is described below.

Giannios & Uzdensky (2019) (hereafter GU19) have modelled the transition from magnetically to kinetically dominated regimes in the flow of a relativistic jet due to the magnetic reconnection of fields of opposite polarity normal to the jet axis, referred as stripes. Magnetic reconnection is regarded as the most efficient mechanism to allow magnetic energy dissipation into heating, kinetic energy as well as particle acceleration. In their scenario, the magnetic stripes originate in the accretion disk where reversed fields are due to turbulent dynamo driven by the magneto-rotational instability (MRI). As they emerge, the stripes pile up along the jet (perpendicular to the axis),

with a distribution of sizes, in a similar, but much simpler configuration than that of the simulations in [Medina-Torrejón et al. \(2021, 2023\)](#).

GU19 propose that the width l of the stripes in the jet follows a power-law distribution $\frac{dP}{dl} = \frac{1}{(a-1)l_{\min}} (l/l_{\min})^{-a}$, being l_{\min} the minimum stripe width, and that, e.g., tearing mode instability induces magnetic reconnection between the stripes in the jet. As stressed in Section 1, in a realistic scenario, the presence of turbulence driven by any instability that naturally develops in jet, such as kink, Kelvin-Helmholtz, Weibel, and even the MRI in the disk, may drive fast reconnection in the magnetized flow ([Kowal et al. 2009](#); [Kadowaki et al. 2018](#); [Nishikawa et al. 2020](#); [Kowal et al. 2020](#); [Medina-Torrejón et al. 2021](#); [Kadowaki et al. 2021](#); [Medina-Torrejón et al. 2023](#)). In recent work, very high resolution 3D MHD resistive simulations have demonstrated that turbulence is more efficient to drive fast reconnection than tearing mode instability ([Vicentin et al. 2024](#); [García-Morillo & Alexakis 2024](#)). Therefore, in this work, we assume that fast reconnection between the stripes is driven by embedded turbulence (see also section 4.2).

Considering a conical jet with half opening angle θ_j and assuming conservation of the total jet power $L_j = L_B + L_K$, where L_B and L_K are the magnetic and kinetic power, respectively, GU19 derive an analytic model describing the jet bulk motion that converges to an asymptotic Lorentz factor Γ_∞ . We adopt this formalism to assess the physical properties of a jet dissipating magnetic energy by reconnection along the jet flow. Based on this jet model, we parametrise the macroscopic properties within the jet. We assume that particle acceleration by reconnection occurs at the jet's transition region, where it shifts from being magnetically dominated to kinetically dominated, as this is where the most significant energy emission and dissipation are expected. The solutions of the GU19 model give the magnetic dissipation power P_{diss} , and the jet bulk Lorentz factor Γ_j (both in the BH frame), at a distance s from the BH, as:

$$P_{\text{diss}}(s) = L_j \frac{[1 - \chi(\zeta)]^k}{\chi^2(\zeta)} \zeta, \quad (1)$$

$$\Gamma_j(s) = \Gamma_\infty \chi(\zeta), \quad (2)$$

where

$$\zeta = \frac{2\xi_{\text{rec}} s}{l_{\min} \Gamma_\infty^2}, \quad (3)$$

and

$$k = \frac{3a - 1}{2a - 2}. \quad (4)$$

In equations (1)-(3), χ is the bulk Lorentz factor of the jet in units of its terminal value Γ_∞ , ζ (eq. 3) is the dimensionless distance in the jet from the BH, and $\xi_{\text{rec}} = v_{\text{rec}}/v_A$ is the fraction of the reconnection velocity relative to the local Alfvén velocity. This reconnection rate, measured from 3D MHD numerical simulations of turbulence induced reconnection, is $\xi_{\text{rec}} \sim 0.03 - 0.1$ (e.g. [Kowal et al. 2009](#); [Takamoto et al. 2015](#); [Singh et al. 2016](#); [del Valle et al. 2016](#); [Kadowaki et al. 2021](#); [Guo et al. 2019](#); [Medina-Torrejón et al. 2023](#); [Vicentin et al. 2024](#)). Thus we adopt the fiducial value of $\xi_{\text{rec}} = 0.05$ throughout the analysis of this paper (see also section 4.2).

The parameter χ is obtained as solution of the differential equation:

$$\frac{d\chi}{d\zeta} = \frac{(1 - \chi)^k}{\chi^2}, \quad (5)$$

which has the implicit analytic solution:

$$\zeta - \zeta_0 = F(\chi) - F(\chi_0) \quad (6)$$

with

$$F(\chi) \equiv \frac{(1 - \chi)^{3-k}}{k-3} - \frac{2(1 - \chi)^{2-k}}{k-2} + \frac{(1 - \chi)^{1-k}}{k-1}, \quad (7)$$

being (ζ_0, χ_0) the initial conditions of equation (5).

In order to define a particular solution of equation (5), values for the power index a for the distribution of the stripe widths and for the boundary condition (ζ_0, χ_0) should be defined. The value of the power-law index a may depend on the accretion process on to the BH, however it is not well constrained as pointed out by GU19. We note that the solutions to equation (5) are not sensitive to the choice of the value of a for $a \gtrsim 3.5$. In this case the solutions seem to converge to an asymptotic curve (see Figure 1, upper panel). Moreover, with regard to the boundary condition, the solutions to equation (5) are also practically insensitive to the choice of χ_0 at $\zeta_0 = 0$, for $\zeta > 0.1$, as long as $0 \leq \chi_0 \ll 1$, as shown in the lower panel of Figure 1. Thus, to simplify matters and to reduce the number of free parameters, here we consider the values of $\zeta_0 = 0$ (the location of the central engine), $\chi_0 = 0.1$, and $a = 3.5$ in all solutions derived in this paper.

At a distance s , the gas and magnetic energy densities in the flow co-moving frame U'_g and U'_B can be related to the jet kinetic and magnetic power as $L_k = \Gamma_j^2 \pi r_j^2 \beta_j c U'_g$, and $L_B = \Gamma_j^2 \pi r_j^2 \beta_j c U'_B$, respectively, where r_j and $\beta_j = v_j/c$ are the jet cross section and flow velocity at s . Then we estimate the gas density and magnetic field in the flow co-moving frame as:

$$\rho' = \frac{L_j}{\Gamma_\infty^2 \pi r_j^2 \beta_j c^3 \chi(s)}, \quad (8)$$

$$\frac{B'^2}{4\pi} = \frac{L_j [1 - \chi(s)]}{\Gamma_\infty^2 \pi r_j^2 \beta_j c \chi^2}, \quad (9)$$

where $r_j \approx \theta_j s$ is a good approximation for a small jet opening angle θ_j , and χ as a function of s is obtained solving numerically equations (5)-(6).

For calculating the physical quantities P_{diss} , Γ_j , and B' from eqs. (1)-(9), we need to define the values of Γ_∞ , L_j , and l_{\min} . Given the lack of knowledge about Γ_∞ , L_j , and l_{\min} for the source TXS 0506+056, we leave these quantities as free parameters with the following constraints. We take the total jet power as a factor λ of the BH Eddington luminosity $L_j = \lambda L_{\text{Edd}}(M_{\text{BH}})$, with $10 < \lambda < 100$, as required by hadronic models (e.g. [Zdziarski & Botcher 2015](#); [Liodakis & Petropoulou 2020](#)). Here we fix the mass of the central SMBH to $M_{\text{BH}} = 3 \times 10^8 M_\odot$ following [Padovani et al. \(2019\)](#). The minimum width of the stripes is constrained within the range of $100R_g < l_{\min} < 1000R_g$, being $R_g = GM_{\text{BH}}/c^2$ the gravitational radius of the central BH, as pointed out by GU19. In addition, the terminal Lorentz factor of the jet flow is taken within the range of $\Gamma_\infty \simeq 30 - 60$, which is compatible with the values typically constrained by observations of blazar jets (e.g. [Hovatta et al. 2009](#); [Lister et al. 2019](#)).

3 MULTI-MESSENGER EMISSION POWERED BY MAGNETIC RECONNECTION

The fast magnetic reconnection driven by turbulence among the magnetic stripes which sustain the stationary jet structure in the model of GU19 (Section 2) can also accelerate particles like electrons and ions to relativistic energies through Fermi-like acceleration process followed by drift acceleration ([de Gouveia Dal Pino & Lazarian 2005](#); [Medina-Torrejón et al. 2021, 2023](#)). In Section 4.2, we discuss these

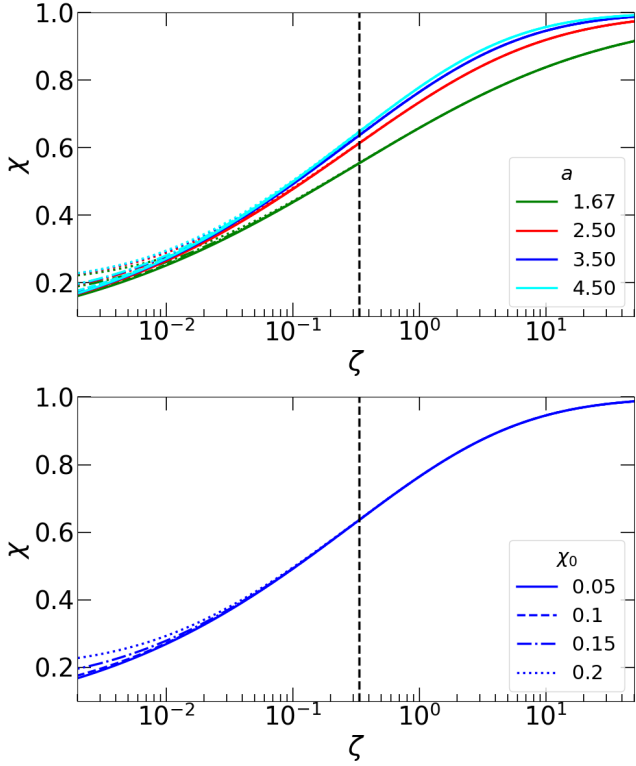


Figure 1. Solutions to eq. (5) giving $\chi = \Gamma_j/\Gamma_\infty$ (jet bulk Lorentz factor in units of its terminal value) as a function of the dimensionless distance to the BH ζ (defined in eq. 3). Top: Curve solutions corresponding to different values of the power-law index a for the distribution of the stripes (see the text), and for different initial values of χ_0 at $\zeta_0 = 0$. Bottom: The family curve solution corresponding to $a = 3.5$ is plotted alone in this panel to illustrate the effect of different choices of χ_0 . In both panels, the dashed vertical line indicates the location where the peak of magnetic power dissipation occurs (see the text).

acceleration regimes in detail and show how they influence the emission of the particles and the resulting SED. We find that acceleration is dominated by the Fermi process. If these non-thermal particles carry a non-negligible fraction of the magnetic dissipation power P_{diss} (see equation 1), their energy losses can account for the observed quiescent emission from blazars (e.g. Medina-Torrejón et al. 2021, 2023).

Flares or temporary enhanced jet emission could be produced by an excess of particle injection in a localized region of the jet (Aharonian et al. 2007; Ackermann et al. 2016; Britto et al. 2016; IceCube Collaboration et al. 2018b,a) over the stationary state of particle injection. To interpret blazar flares as an excess over its quiescent emission, for simplicity here we calculate the emission of non-thermal stationary distributions of relativistic electrons (e) and protons (p), $N_{e,p}(E)$ (i.e., the number of particles with energy E per unit volume). This is calculated in the frame of an approximately spherical emitting region, hereafter referred to as the blob, located in the jet's transition zone from magnetically to kinetically dominated, with a radius r_b . We constrain the energy distributions of the relativistic particles so that their kinetic luminosity (in the BH frame) represents a fraction η_i ($i = e, p$) of the local magnetic dissipation by reconnection power (see Section 2):

$$L_i = \eta_i P_{\text{diss}}(s) = \Gamma_j^2(s) \pi r_b^2 \beta_j c U_i' \quad (10)$$

with U_i' being the energy density of accelerated particles (electrons or protons) in the frame of the emitting reconnection blob, given as:

$$U_i' = \int_{E_{0,i}}^{\infty} dE_i' E_i' N_i'(E_i'), \quad (11)$$

where N_i' is the number of particles per unit energy, per unit volume, in the co-moving frame of the emission region.

For relativistic protons, we approximate their stationary particle energy distribution as

$$N_p' = t_p'(E_p') Q_p'(E_p'), \quad (12)$$

where E_p' is the proton energy, t_p' is the proton injection time and Q_p' is the stationary proton injection function (particles per unit energy, per unit volume, per unit time), in the blob frame. The proton injection time is taken as

$$t_p' = \min \{t_{p,\text{cool}}, t_{\text{acc}}\}, \quad (13)$$

where $t_{p,\text{cool}}$ is the particle cooling time, and t_{acc} is the proton acceleration time, which is described in Section 4.2.

The particle cooling time $t_{p,\text{cool}}$ is taken as the inverse of the total cooling rate:

$$t_{p,\text{cool}}^{-1} = \left[t_{p\gamma}^{-1}(E_p') + t_{\text{B-H}}^{-1}(E_p') + t_{p,\text{syn}}^{-1}(E_p') \right]^{-1}, \quad (14)$$

being, $t_{p\gamma}^{-1}$, $t_{\text{B-H}}^{-1}$, and $t_{p,\text{syn}}^{-1}$ the proton cooling rates due to photo-pion production, Bethe-Heitler pair production, and synchrotron radiation, respectively¹. We refer to Appendix 6 for the mathematical expressions that we employ for the cooling rates of equation (14).

We parametrise the proton injection function Q_p' (particles per unit energy, per unit volume, per unit time) in eq. (12) as a stationary power-law energy distribution with squared exponential cut-off:

$$Q_p' = Q_0'(E_p'/E_{p,0}')^{-\alpha_p} \exp \left\{ - \left(E_p'/E_{p,\text{max}}' \right)^2 \right\}, \quad (15)$$

where we set $E_{p,0}' = 1$ GeV as the minimum energy of the proton distribution, α_p is the proton power-law index, $E_{p,\text{max}}'$ is the maximum energy of the proton population (see Section 4.2), and the normalisation factor Q_0' is obtained through equations (10-11).

For the parameter space explored in this work, the SSC cooling of primary electrons mostly falls in the Thompson regime, and the cooling time scale due to synchrotron and SSC radiation of the accelerated electrons is always much shorter than the adiabatic time scale (Section 4.3). Thus, we parametrise the stationary energy distribution of primary electrons (in units of particles per volume per energy) as a single power-law with squared exponential cutoff:

$$N_e' = N_{e,0}' \left(E_e'/E_{e,0}' \right)^{-n_e} \exp \left\{ - \left(E_e'/E_{e,\text{max}}' \right)^2 \right\}, \quad (16)$$

where $E_{e,0}'$ and $E_{e,\text{max}}'$ are the minimum and maximum energy of the electron population, respectively, and we set $n_e = \alpha_p + 1$. This choice for the index n_e is motivated by a scenario where electrons and protons are energised by the same acceleration process. Finally, the normalisation factor $N_{e,0}'$ of the electron distribution is also obtained through eq. 11.

¹ We note that the cooling of CR protons due to proton-proton reactions is generally not relevant in blazar jets and specially in this system due to the very low density of the thermal plasma.

4 MODEL FOR THE TXS 0506+056 MM FLARE

As stressed, here we interpret the MM SED data set related to the 2017 neutrino flare of TXS 0506+056 (IceCube Collaboration et al. 2018b), assuming a lepto-hadronic emission powered by magnetic reconnection in the blazar jet (see Sections 2 and 3). The broadband SED of the source associated with the detection of the neutrino event IC-170922A is shown in Figure 7, adapted from IceCube Collaboration et al. (2018b). The fluxes indicated by the upper limits at [0.3–3] PeV, with solid and dashed lines, are consistent with one neutrino detection within 0.5 years and 7.5 years, respectively. The data points from radio to VHE gamma-rays present the quasi-simultaneous SED observed from the source. The radio data points, plotted in grey, are not intended to be explained by the emission scenario discussed here, as this emission in blazars is generally attributed to a much larger-scale region in the jet.

We particularly work out the hybrid radiation scenario where CR protons account for the production of HE neutrinos in which the high-energy EM bump of the blazar spectrum is mostly accounted by Synchrotron-self-Compton (SSC) emission of primary electrons. Under this radiation scenario, we expect partial contributions from CR protons to the EM emission at X-rays and VHE gamma rays through electromagnetic cascades, as exhibited by hybrid models (Cerruti et al. 2019; Gao et al. 2019).

4.1 The location of the emission region

We combine the aforementioned SSC radiative condition with the jet model described in Section 2 to constrain the location range in the jet where the conditions are fulfilled to produce the observed MM emission. Requiring that the bumps of the blazar spectrum peaking at $E_{\text{pk},\ell}$ and $E_{\text{pk},h}$ are produced mostly by synchrotron and SSC radiation, respectively, we first constrain the possible values of B' and Γ of the emission region as follows.

We note that in the co-moving frame of the emission region, relativistic electrons with Lorentz factor γ'_e produce synchrotron emission with frequency $\nu'_{\text{syn}} = \gamma_e'^2 \nu'_L$, being $\nu'_L = eB'/(2\pi m_e c)$ the Larmor frequency, and e the electron charge (Longair 2011). The associated SSC photons boosted by the same electrons emit at frequency $\nu'_{\text{ssc}} \approx \gamma_e'^2 \nu'_{\text{syn}}$ (Ghisellini 2013). Thus, the frequencies of synchrotron and SSC peaks can be related as $\nu'_{\text{syn}} \approx (\nu'_{\text{ssc}}/\nu'_{\text{syn}})\nu'_L$. On the other hand, the synchrotron and SSC frequencies in the observer frame can be approximated as $\nu_{\text{syn}} = \nu'_{\text{syn}}\Gamma_j/(1+z)$ and $\nu_{\text{ssc}} = \nu'_{\text{ssc}}\Gamma_j/(1+z)$, respectively. Therefore, given the energies of the low and high energy bumps of the blazar spectrum, the co-moving magnetic field and the jet bulk Lorentz factor at the emission region can be constrained as:

$$B' = \frac{E_{\text{pk},\ell}^2 m_e c (1+z)}{E_{\text{pk},h} e \hbar \Gamma_j}. \quad (17)$$

In this equation, $E_{\text{pk},\ell}$ and $E_{\text{pk},h}$ are the low and high energy blazar SED bumps, respectively, at the observer's frame. We note that SED models with energies values in the interval of $E_{\text{pk},\ell} \in [5, 15]$ eV are consistent with observed low energy blazar bumps and, at the same time, have suitable target photons to produce high energy neutrinos peaking at \sim PeV energies (in the observer's frame). On the other hand, the observed high energy bump of TXS 0506+056 is consistent with $E_{\text{pk},h} \sim [0.5 - 2]$ GeV interval (IceCube Collaboration et al. 2018b).

In order to find jet solutions and derive the location of the emission region (s_{em}) which are consistent with the constraint given by eq. 17, we employ equations 6 to 9. This combination results:

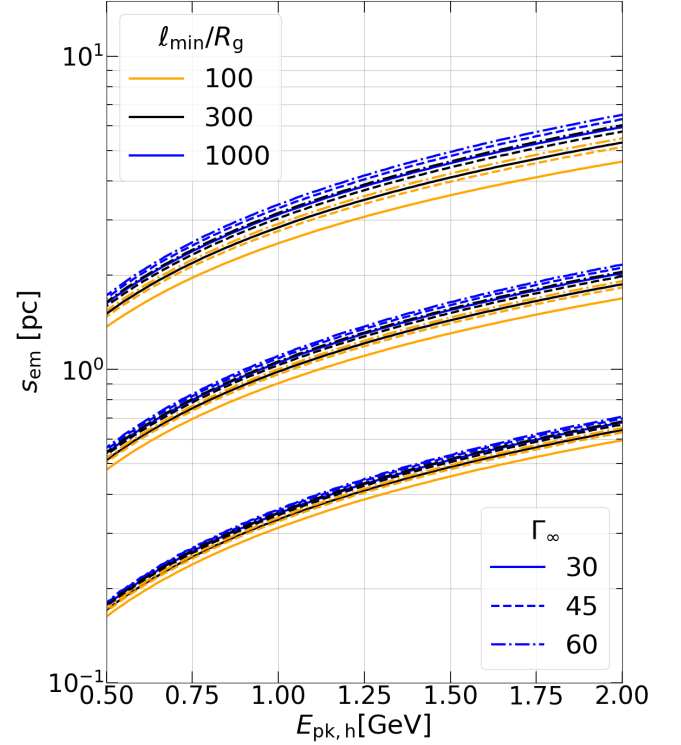


Figure 2. Constraining the location of the emission region along the jet. We display the solutions to equations 18-19, for the possible location s_{em} . Curves plotted with different colours and line styles correspond to different values of minimum length of the stripes l_{min} and of the terminal Lorentz factor Γ_{∞} of the jet flow, as indicated. The lower, middle, and upper groups of curves correspond to total jet powers of $L_j = 1.5, 15$ and $150L_{\text{Edd}}$, respectively.

$$s_{\text{em}} = \frac{l_{\text{min}}\Gamma_{\infty}^2}{2\xi_{\text{rec}}} [F(\chi_{\text{em}}) - F(\chi_0)], \quad (18)$$

$$\chi_{\text{em}} = 1 - \frac{c\beta_{\text{em}}}{L_j} \left[\frac{E_{\text{pk},\ell}^2 m_e c (1+z)}{E_{\text{pk},h} 2e\hbar} \theta_j s_{\text{em}} \right]^2, \quad (19)$$

where $\beta_{\text{em}} = \left(1 - (\Gamma_{\infty}\chi_{\text{em}})^{-2}\right)^{1/2}$.

In Figure 2, we display the solutions for the emission region, s_{em} , as a function of the observed energy range of the high bump of the TXS 0506+056 SED within the interval $E_{\text{pk},h} \in [0.5, 2]$ GeV, fixing $E_{\text{pk},\ell} = 10$ eV. The different colours and line styles of the curves correspond to different values of l_{min}/R_g (100, 300, and 1000), and Γ_{∞} (30, 45, and 60), as indicated. They are calculated for three values of the jet power $L_j = 1.5, 15$ and $150L_{\text{Edd}}$.

Considering $L_j = 150L_{\text{Edd}}$ from Figure 2, we see that the possible locations for the emission regions can be limited within the interval of $\Delta s_{\text{em}} \sim [1.5 - 6]$ pc. For this length range, the jet dissipation power P_{diss} , magnetization $\sigma = L_B/L_K$, magnetic field B' , and Γ_j , fall within the range of values indicated by the pink shaded regions in Figure 3.

Based on the parametric space defined above, we construct the lepto-hadronic SED for TXS 0506+056. To achieve this we consider the emitting blob, described in section 3, moving downstream with the jet flow at three different positions, which are illustrated in Figure 4. At each position along the jet, the blob radius is constrained by the

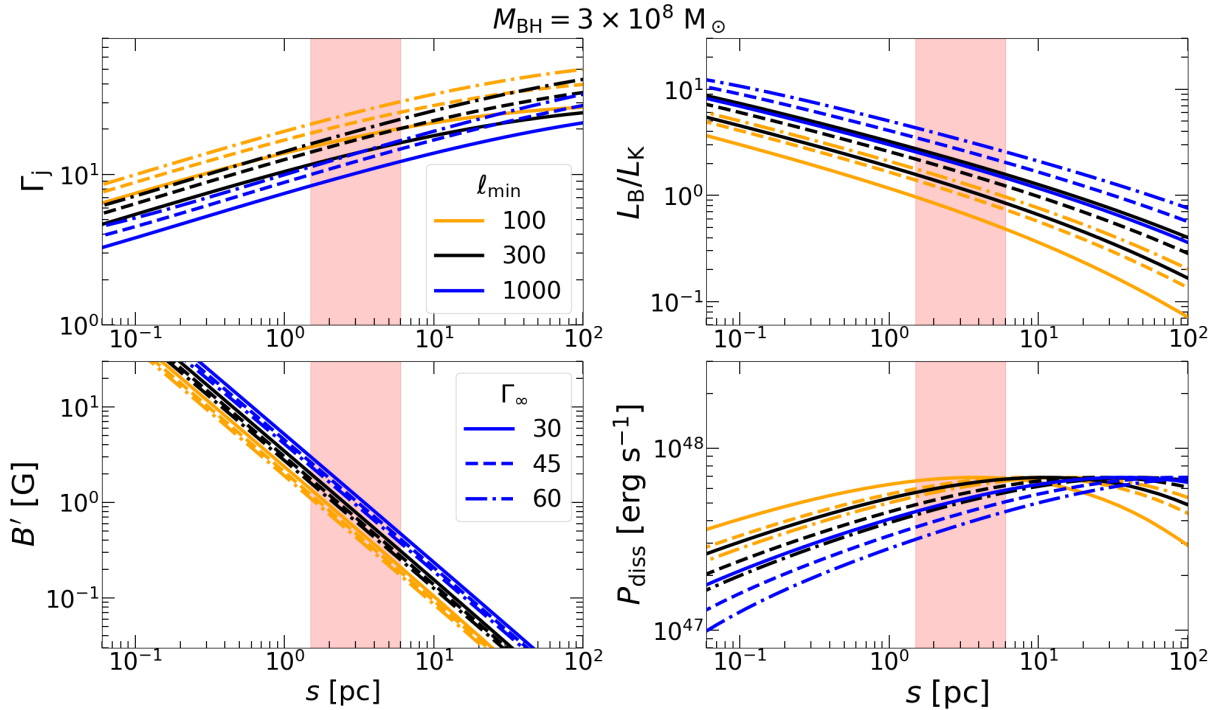


Figure 3. Jet properties given by the stripe jet model (Section 2) as functions of the distance from the SMBH. All curves in this plot are calculated assuming an SMBH of $M_{BH} = 3 \times 10^8 M_{\odot}$, and a jet total power of $L_j = 150L_{Edd}(M_{BH})$. The pink shaded regions indicate the location interval compatible with the constraint obtained from Figure 2 for the possible emission regions (see the text). The different curve styles in this plot are calculated assuming different values for the terminal Lorentz factor of the jet flow as labelled. Orange, black and blue colours indicate curves obtained assuming $l_{min}/R_g = 100, 300$, and 1000 , respectively ($R_g = GM_{BH}/c^2$). These intervals will serve as guidelines for modelling the MM SED of TXS 0506+056.

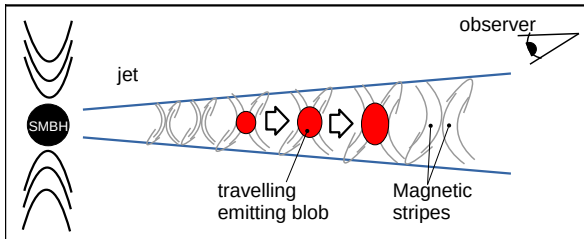


Figure 4. Sketch of the emitting blob as it moves downstream the expanding jet. The three different positions indicate the regions at which the SED of TXS 0506+056 is evaluated in Figure 7. The blob is assumed to be spherical in the comoving frame.

causality condition given by the minimum variability time interval Δt_v observed during the 2017 flare. This results

$$r_b = f_v \frac{c \Delta t_v \Gamma_j}{(1+z)}, \quad (20)$$

where f_v is a dimensionless free parameter $f_v \leq 1$, and we take $\Delta t_v \approx 1$ day, which is consistent with the minimum variability of the source observed at X-rays (Keivani et al. 2018).

4.2 Particle acceleration by magnetic reconnection and the maximum energy of the particles

As remarked in Section 1, during the Fermi regime of particle acceleration through reconnection, it is expected that particles experience an exponential growth in energy over time (e.g. de Gouveia Dal Pino & Lazarian 2005). 3D MHD simulations with test particles align with

this expectation, revealing a reconnection acceleration time with a weak dependence on particle energy, expressed as $t_{acc} \propto E^{-0.2-0.1}$, specially for relativistic reconnection velocities (e.g. del Valle et al. 2016; Liu et al. 2017; Medina-Torrejón et al. 2021, 2023). In a recent study, Xu & Lazarian (2023) revisited the earlier work by de Gouveia Dal Pino & Lazarian (2005), and derived the following condition for fastest acceleration time (in the Fermi regime) within a turbulence-induced magnetic reconnection layer of reconnection velocity v_{rec} and thickness Δ :

$$t_{acc} \sim \frac{4\Delta}{cd_{ur}} \quad (21)$$

where

$$d_{ur} \approx \frac{2\beta_{rec}(3\beta_{rec}^2 + 3\beta_{rec} + 1)}{3(\beta_{rec} + 0.5)(1 - \beta_{rec}^2)}, \quad (22)$$

with $\beta_{rec} = v_{rec}/c$ and c the light speed. This relation has been recently successfully confirmed by means of 3D MHD simulations of turbulent relativistic jets with test particles (de Gouveia Dal Pino & Medina-Torrejón 2024).

In this work Δ corresponds to the size of the acceleration region which in turn is given by the blob size $\Delta \sim 2r_b$. We take from the numerical simulations $v_{rec} \approx 0.05v_A$ (e.g. Medina-Torrejón et al. 2021, 2023), where the Alfvén speed in the relativistic regime is:

$$v_A \approx \frac{v_{A,0}}{\sqrt{1 + \left(\frac{v_{A,0}}{c}\right)^2}} \quad (23)$$

where $v_{A,0} = B'/\sqrt{4\pi\rho'}$. For the jet model adopted in this work,

$v_{A,0}$ can be calculated through equations (8) and (9), giving:

$$v_{A,0} = c \sqrt{\frac{1-\chi}{\chi}}, \quad (24)$$

where χ depends on the jet location as given by equations (5)–(6).

This acceleration time is independent of the particles energy, as expected in the Fermi regime for constant reconnection speed, and which is in agreement with the above mentioned simulations (see also de Gouveia Dal Pino & Medina-Torrejón 2024).

This regime of acceleration will persist until a threshold energy which is attained when the particles Larmor radius becomes larger than the thickness of the reconnection layer, $r_L \simeq 2r_b$. For instance, for the parameters of the inner blob position, this implies a proton energy threshold $E_{th} \simeq 10^{19}$ eV (Figure 5). This value is also consistent with those obtained from 3D MHD numerical simulations of relativistic jets with test particles for similar background magnetic fields, in the absence of radiative losses (Medina-Torrejón et al. 2021).

In a subsequent drift regime, occurring after particles have attained the threshold energy and exited the reconnection zones, the energy growth with time becomes strongly dependent on the energy and therefore, slower. The acceleration time in this regime is approximately described by the equation $t_{acc,drift} \simeq E_p / (qB'v_{rec})$ (de Gouveia Dal Pino & Kowal 2015; del Valle et al. 2016; Zhang et al. 2023b). The MHD numerical simulations with test particles have confirmed that the extended acceleration time observed in the drift regime is attained only for $E_p > E_{th}$ (Kowal et al. 2012; del Valle et al. 2016; Medina-Torrejón et al. 2021).

In Figure 5, we compare the particle acceleration time by magnetic reconnection with the total proton radiative cooling time (eq. 14), both calculated in the plasma frame, in three different positions along the jet. These positions correspond to those at which the SED is calculated in Figure 7 (Section 4.3).

The maximum possible energy of the protons in the emission blob, $E'_{p,max}$ (eq. 15), in Figure 5, is given by the value at which

$$t'_{acc} = t'_{cool}.$$

We observe from the very high energy threshold found for the Fermi regime in the three diagrams of Figure 5 (indicated by the maximum extension of the blue lines) that this regime will dominate particle acceleration within the blob. We also note that the obtained values of $E'_{p,max}$ are well below this threshold energy (E_{th}), and protons with energies $E_p > E'_{p,max}$ will lose their energy radiatively inside the emission blob.

Similarly, the maximum energy for the electrons, $E'_{e,max}$ (eq. 16), can be also obtained from the balance between the total radiative cooling time and the reconnection acceleration time. Nevertheless, it is worthy noting that the supra-thermal electrons in the acceleration region will start Fermi acceleration at scales much smaller than that of the protons. This is due to their much smaller Larmor radius for energies of the order of their rest mass. They will start interacting with very tiny magnetic fluctuations at the acceleration zone, effectively in reconnection structures with thickness $\gtrsim r_{L,e}$. At these scales, Δ in eq. 21 results an acceleration time for the electrons which is much smaller than that evaluated for protons in Figure 5. From the ratio between the electron and the proton momentum equations in the relativistic regime, one can easily demonstrate that $t'_{acc,e}/t'_{acc,p} \sim m_e/m_p$ (see also Khiali et al. 2015; Khiali & de Gouveia Dal Pino 2016; Medina-Torrejón et al. 2021).

Figure 6 presents the estimated Fermi acceleration time, as calculated from Eq. 21 and adjusted by the mass ratio factor, alongside the synchrotron and SSC loss times for electrons at the three different

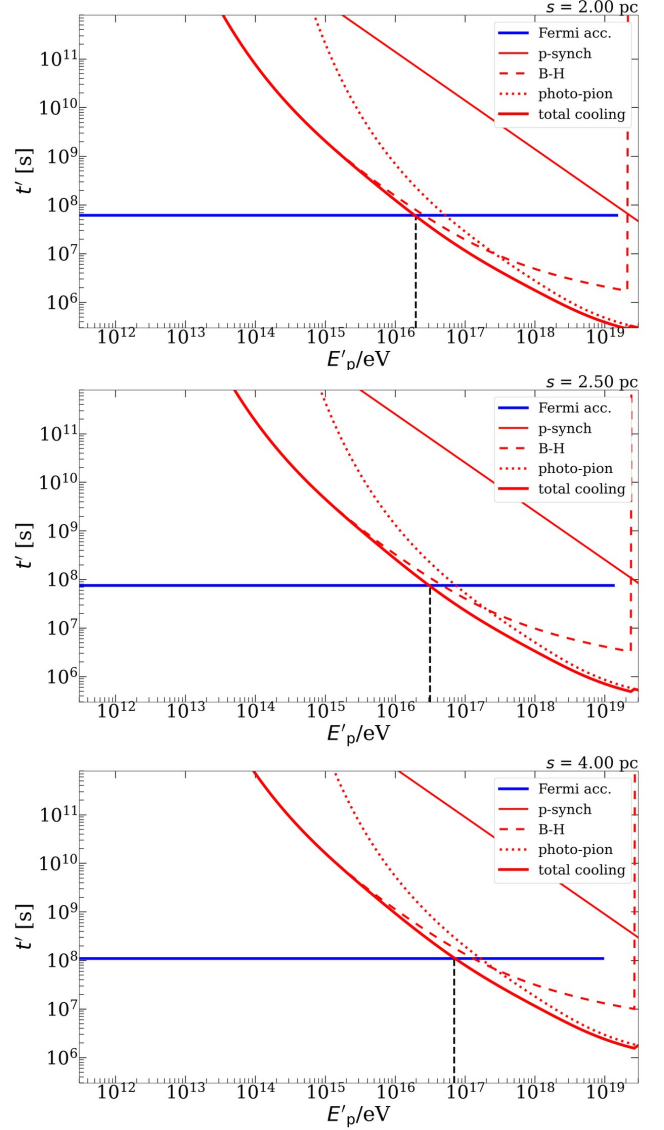


Figure 5. Cooling time of the CR protons (source frame) which produce the hadronic emission components of the SED spectrum in Figure 7, calculated for three different positions of the emission blob in the jet, $s = 5$ (top), 8 (middle) and 10 pc (bottom panel). The different cooling processes (photo-pion production, photo-pair (B-H) production, and synchrotron) are displayed with thin curves of different line styles as indicated, whereas the total cooling time is plotted by the red thick curve. We over-plot the proton acceleration time due to magnetic reconnection in the Fermi acceleration regime (blue line). The resulting total radiative cooling time curve is intercepted by the acceleration time curve at the vertical dashed black line. This indicates the maximum energy required in our modelling to produce the theoretical SED sequence of Figure 7 (see text for details).

locations of the emitting blob in the jet. The vertical grey dashed line on the right denotes the maximum electron energy, $E_{e,max}$, calculated to match the observed synchrotron bump in the SED of TXS 0506+056. Notably, the reconnection acceleration time intersects the synchrotron cooling time curves near this maximum energy, indicating that the acceleration model aligns well with the maximum electron energy inferred from observations.

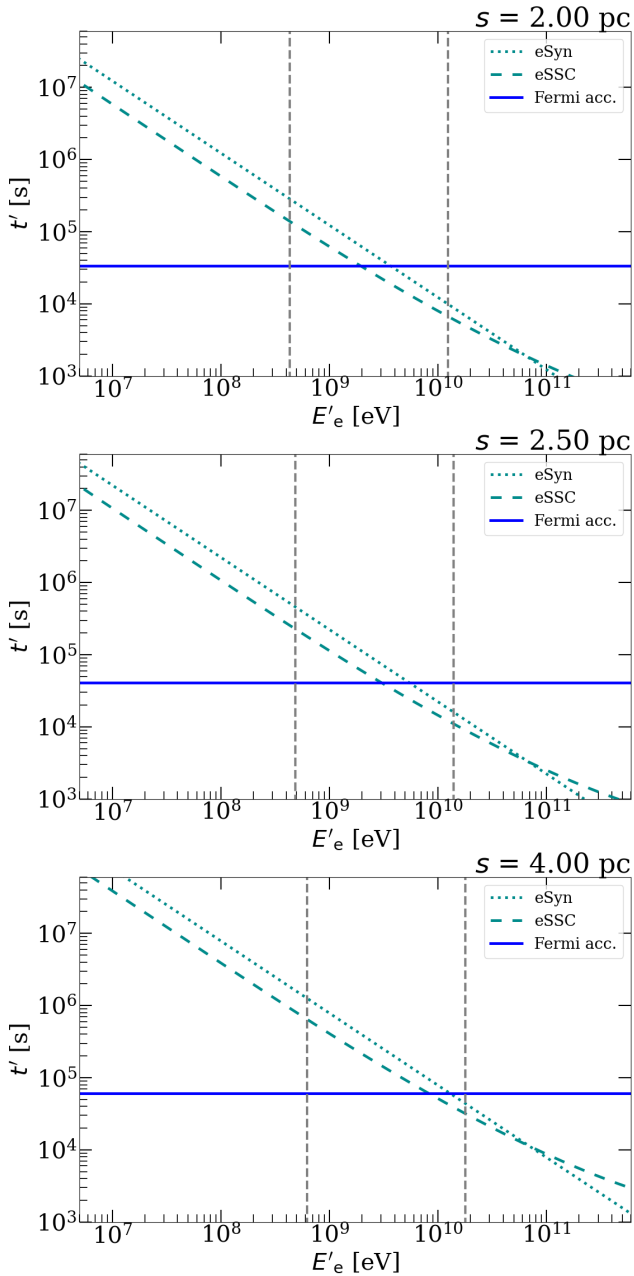


Figure 6. Cooling times (green lines) and reconnection acceleration time in the Fermi regime (blue line) of accelerated electrons in the frame of the emitting blob for the SED sequence presented in Figure 7. The vertical dashed black lines indicate the minimum (left) and the maximum energy (right) of the electron population evaluated directly from the synchrotron peak around 3 eV of the SED of TXS 0506+056.

4.3 Multi-messenger SEDs

We derive lepto-hadronic SED profiles from the emission region, which is a spherical blob moving downstream in the jet (Figure 4). This region has uniform macroscopic properties, parametrized according to the GU19 model, as described in Section 2. The properties of the blob are then calculated as function of the jet longitudinal distance s .

We probe the MM emission of TXS 0506+056 employing the leptonic and hadronic processes described in Section 4.1 and Ap-

Table 1. Free and calculated parameters from the jet emission model at each position $s_{\text{em},i}$ of the blob, leading to the SED curves of Figure 7. Quantities in blue with the (*) label are the derived parameters from model.

Parameter	$s_{\text{em},1}$	$s_{\text{em},2}$	$s_{\text{em},3}$
$\lambda = L_j/L_{\text{Edd}}$	1.5E2	1.5E2	1.5E2
$f_\ell = \ell_{\text{min}}/R_g$	1.0E3	1.0E3	1.0E3
Γ_∞	45	45	45
s [pc]	2.0	2.5	4.0
f_v	0.672	0.753	0.948
α_p	1.7	1.7	1.7
η_p	0.75	0.65	0.50
η_e	2.2E-4	2.5E-4	3.2E-4
$E'_{e,0}$ [MeV]	4.32E2	4.85E2	6.22E2
$E'_{e,\text{max}}$ [GeV]	1.25E1	1.40E1	1.80E1
L_j [erg/s] *	5.67E48	5.67E48	5.67E48
$\chi(s)$ *	0.24	0.26	0.29
$\Gamma_j(s)$ *	10.8	11.6	13.2
$B'(s)$ [G] *	1.79	1.33	0.71
$L_B/L_K(s)$ *	3.15	2.90	2.41
v_{rec}/c *	4.36E-2	4.31E-2	4.20E-2
$r_b = f_v \frac{c\Delta r_j \Gamma_j(s)}{(1+z)}$ [cm] *	1.41E16	1.69E16	2.43E16
$E'_{p,\text{max}}$ [PeV] *	1.98E1	3.14E1	5.58E1

pendix 7 at three different locations within an interval $\Delta s \rightarrow [2 - 4]$ pc. This is within the range Δs_{em} constrained in Figure 2 and Figure 3 (pink band).

Each SED of the sequence shares the same values for the parameters L_j , Γ_∞ , and l_{min} . Then, each SED is obtained by freely tuning the other parameters f_v , η_e , η_p , α_p , $E'_{e,0}$, and $E'_{e,\text{max}}$ to match the TXS 0506+056 SED data set (see Sections 3 and 4.2). The assumed and derived parameters of the emitting blob at the different positions along the jet are given in Table 1.

We show in Figure 7 the sequence of MM SEDs as the blob moves downstream. The SED with the peak of the neutrino flux closest to the Icecube upper limits is obtained at the blob location closest to the jet core ($s = 2$ pc), corresponding to a region of higher magnetization $\sigma \equiv L_B/L_K$ (top panel). This SED does not reproduce yet the VHE gamma-rays (> 100 GeV) of the data set, only the high state peak around 1 GeV, as expected from the observations.

As the blob moves to larger distances s , the peak of the neutrino flux moves towards higher energies, and hence outside the sensitivity energy interval of the Icecube detector, while the flux of VHE γ -rays ($E > 100$ GeV) is enhanced (middle diagram of Figure 7), and finally, when the blob moves to $s = 4$ pc, the largest position within the considered range (bottom panel of Figure 7), the SED matches the observed EM data (including the VHE gamma-rays), but exhibits the lowest flux of neutrinos.

The behaviour of this SED sequence is consistent with the arrival time delay between the HE neutrino observed in the direction of TXS 0506+056 (which is simultaneous to the high state emission of the source around ~ 1 GeV), and the subsequent appearance of the VHE γ -ray signal, followed by the loss of neutrino detection.

The time interval comprising the sequence of SEDs shown in Figure 7 can be estimated as follows. As the blob moves downstream, it suffers relativistic beaming with apparent superluminal motion, that must be corrected according to (e.g. Rees 1966; de Gouveia dal Pino & Opher 1991, and references therein)

$$\Delta t_{\text{ap}} = \Delta t(1+z)[1 - \bar{\beta}_j \cos(\theta_j)] \approx \Delta t \frac{(1+z)}{\bar{\Gamma}_j^2} \quad (25)$$

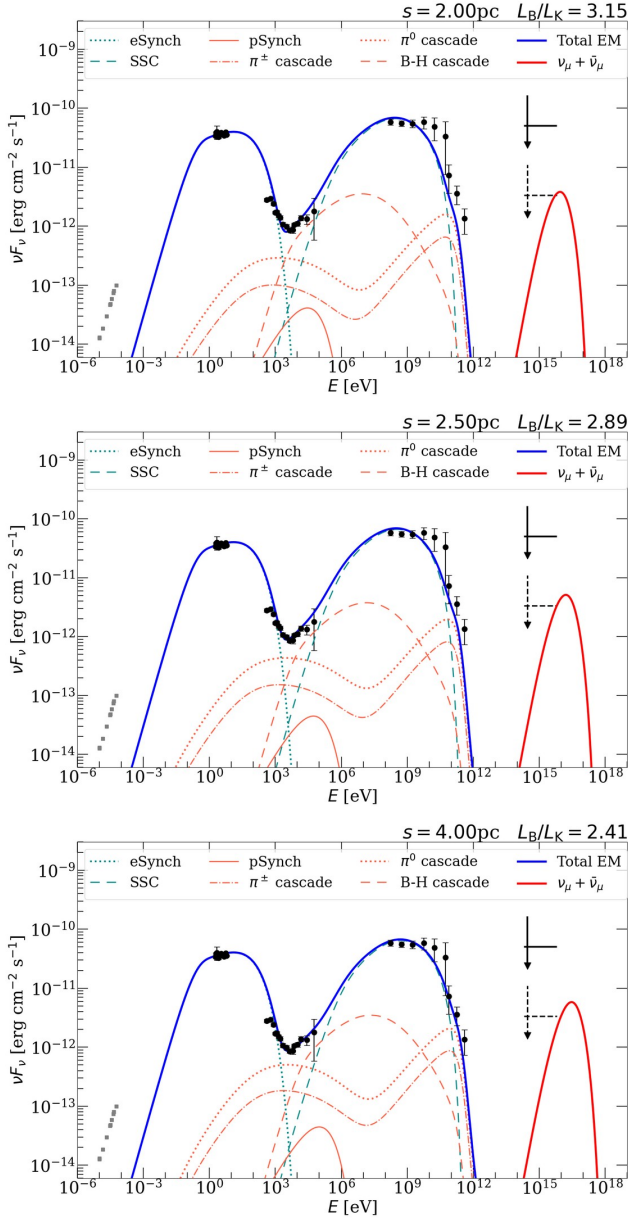


Figure 7. Blazar MM spectrum profiles computed based on lepto-hadronic emission powered by magnetic reconnection in the jet. The curves in this Figure are calculated by the jet model described in Section 2 together with the lepto-hadronic radiation model detailed in Section 3. The over-plotted data points correspond to the observed MM SED of the 2017 neutrino flare from the source TXS 0506+056, adapted from [IceCube Collaboration et al. \(2018b\)](#). The red thick curve in each panel plots the all flavour neutrino emission whereas the blue thick curve plots the total emission composed by radiation of leptonic (cyan curves) and hadronic (crimson curves) origin. The emission profiles in each panel correspond to different locations s of the jet as labelled. The magnetisation $\sigma = L_B/L_K$ label in each panel is a derived quantity associated to the location s and calculated through the jet model (see text).

where the last approximation is obtained considering a second order expansion of $\cos(\theta_j)$ and $\theta_j \sim 1/\bar{\Gamma}_j$. In eq. 25, Δt is the time interval between the emission sequence within the length interval Δs , as measured in the BH frame. We evaluate this time interval as $\Delta t = \Delta s/\bar{v}_j \sim \Delta s/c$, being $\bar{v}_j = c\bar{\beta}_j$ the average velocity of the jet flow within Δs . Using $\Delta s = 0.5\text{pc}$, $\bar{\Gamma}_j \sim 11$, and $z \approx 0.34$, eq. 25 gives an observed time interval of $\Delta t_{ap} \sim 6.4$ days between the first and the second SEDs of Figure 7. This is consistent with the observed time elapsed between the neutrino and the VHE energy flare (> 100 GeV) of TXS 0506+056 2017 ([IceCube Collaboration et al. 2018b](#)). Likewise, the total time interval between the first and the last SED in Figure 7, $\Delta t_{ap} \sim 26$ days, is compatible with an observed persistence of the VHE emission and the disappearance of the neutrino signal in the 2017 event.

5 SUMMARY AND DISCUSSION

In this paper, we model the multi-messenger association of the 2017 neutrino flare from the blazar TXS 0506+056 as due to magnetic dissipation in the blazar jet, and derive the MM emission as driven by magnetic reconnection. We adopt a single-zone lepto-hadronic model, where the emission region is represented by a spherical blob moving downstream along with the expanding jet flow, producing the expected observational signals at multiple locations.

The SEDs derived are based on the following considerations:

- (i) The mass of the central BH is $\sim 3 \times 10^8 M_\odot$;
- (ii) The moving emission blob is located at the jet's transition region from magnetically to kinetically dominated, where particle acceleration by magnetic reconnection is expected to be the primary mechanism;
- (iii) There is no influence from external low-energy photons on the emission volume and hence the synchrotron photons of the accelerated electrons internally provide the target radiation field for inverse Compton (IC) scattering, photo-hadronic interactions, and γ -ray attenuation within the emission volume;
- (iv) The high energy peak ($E_{pk} \sim 1$ GeV) of the blazar spectrum is dominated by the SSC emission of the primary electrons;
- (v) The macroscopic properties of the emission volume, such as the local magnetic field, the jet bulk Lorentz factor, and the magnetic dissipation power are parametrised as functions of the jet propagation axis s , following the model of GU19.

Combining the conditions (iv) and (v), we have constrained the possible locations of the flare emission in the jet within the range $\Delta s \sim [2 - 4]$ pc, assuming a BH of $M_{\text{BH}} = 3 \times 10^8 M_\odot$ launching a jet with total power of $L_j = 150L_{\text{Edd}}(M_{\text{BH}})$ (see Figures 2 and 3). We then calculated MM SED profiles with the lepto-hadronic model at multiple positions along the range Δs . Comparing the calculated SED models to the SED data set of the 2017 MM flare from TXS 0506+056, we find the following features.

The most intense observable flux of HE neutrinos is produced at the position, within the range Δs , which is closest to the jet core, where magnetisation is highest, as expected. At this position, the SED profile also reproduces the HE state component (~ 1 GeV) of the SED data set. As the emitting blob moves further downstream, the calculated SED is consistent with the observed electromagnetic data including the VHE gamma rays ($E > 100$ GeV) and the farthest position within Δs has the lowest flux of neutrinos (out of the reach of the IceCube instrument). The behaviour of this sequence of emission profiles is consistent with the observed time delay between the arrival of the HE neutrino from the direction of TXS 0506+056 (which is

simultaneous with the high state γ -ray emission at ~ 1 GeV), and the subsequent appearance of the VHE signal.

The time interval corresponding to the covered range Δs of the SED sequence must be corrected for the apparent superluminal motion that the blob suffers when is moved downstream the relativistic jet. With this correction, we find a time delay $\Delta t_{ap} \sim 6.4$ days between the neutrino and the VHE emission which is consistent with the observations (IceCube Collaboration et al. 2018b).

Despite the simplicity of our model, the results suggest that the observed MM emission of TXS 0506+056 could be explained by the sequence of SED profiles obtained from magnetic reconnection power dissipation and acceleration occurring approximately within the distance range of ~ 2 to 4 pc along the jet, away from the central BH.

Future refinement of this model should include a more realistic background jet provided by numerical relativistic MHD simulations (e.g. Medina-Torrejón et al. 2021, 2023; de Gouveia Dal Pino & Medina-Torrejón 2024), as well as the inclusion of radiative transfer and cosmic ray cascading (as in e.g. Rodríguez-Ramírez et al. 2019; Hussain et al. 2023, 2024) to produce more detailed SED description.

ACKNOWLEDGEMENTS

EMdGDP and JCRR acknowledge support from the Sao Paulo State Funding Agency FAPESP (grants 2013/10559-5, 2017/12188-5, and 2021/02120-0). JCRR also acknowledges support from Rio de Janeiro State Funding Agency FAPERJ (grant E-26/205.635/2022) and EMdGDP the support from CNPq (grant 308643/2017-8). MVdV is supported by FAPESP Grants 2019/05757-9 and 2020/08729-3. JCRR would like to thank Pankaj Kushwaha for useful discussions at the first steps of this work. JCRR made use of Sci-Mind servers machines developed by the CBPF AI LAB team and would like to thank C. R. Bom, P. Russano and M. Portes de Albuquerque for all the support in infrastructure matters.

DATA AVAILABILITY

The simulated data generated during this study are available upon request to the authors.

6 APPENDIX A: TIME SCALES OF PARTICLE ENERGY LOSSES

The cooling time scale of a particle i (=proton, electron, positron) with energy E_i is taken as the inverse of the rate of the cooling process.

In the present emission model, the cooling rate (s^{-1}) of a charged particle i due to synchrotron radiation is calculated as:

$$t_{\text{syn}}^{-1}(E_i) = \frac{P_{\text{syn,tot}}}{E_i}, \quad (26)$$

with

$$P_{\text{syn,tot}} = \frac{4}{3} \left(\frac{m_e}{m_i} \right)^2 \sigma_{\text{T}} c U_{\text{B}} \left(\frac{E_i}{m_i c^2} \right)^2, \quad (27)$$

being the radiated power of the particle, and $U_{\text{B}} = B^2/(8\pi)$ magnetic energy density of the of the emission region.

We also consider the inverse compton (IC) scattering for electrons and positrons, for which the rate is calculated as

$$t_{\text{IC}}^{-1} = \frac{1}{E_e} \int_{\epsilon_{s,m}}^{\epsilon_{s,M}} d\epsilon_s \int_{\epsilon_s}^{\frac{gE_e}{1+g}} dE_\gamma, \frac{2\pi r_0^2 m_e^2 c^5}{E_e^2} \frac{n_{\text{ph}}^{\text{syn}}}{\epsilon_s} F(\epsilon_c, \epsilon_{\text{syn}}, E_e) \quad (28)$$

with $g = 4\epsilon_s E_e / (m_e c^2)^2$, and

$$F(\epsilon_c, \epsilon_{\text{syn}}, E_e) = 2q \ln(q) + (1+2q)(1-q) + \frac{(1-q)b^2}{2(1+b)},$$

$$q = \frac{\epsilon_c (m_e c^2)^2}{4\epsilon_s E_e' (E_e' - \epsilon_c)}, \quad b = \frac{\epsilon_c}{(E_e' - \epsilon_c)}. \quad (29)$$

Protons also cool due to their interactions with the target soft radiation, producing positron pairs, thorough the Bethe-Heitler (B-H) process, and producing pions through the photo-pion channel. Both processes occur when the target photons surpass the threshold energies of $\epsilon_{0,\text{BH}} = 2m_e c^2 \approx 1.02$ MeV and $\epsilon_{0,\pi} = 145$ MeV, respectively, in the rest frame of the relativistic proton. Here we calculate the cooling rate due to these photo-hadronic processes as (e.g., Atoyan & Dermer 2003; Romero et al. 2010; Khiali et al. 2015):

$$t_{p\gamma}^{-1}(E_p) = \frac{c}{2\gamma_p^2} \int_{\frac{\epsilon_0}{2\gamma_p}}^{\infty} d\epsilon \frac{n_{\text{ph}}^{\text{syn}}(\epsilon)}{\epsilon^2} \int_{\epsilon_0}^{2\epsilon\gamma_p} d\epsilon' \epsilon' K_{p\gamma} \sigma_{p\gamma}, \quad (30)$$

where $\sigma_{p\gamma}$, and $K_{p\gamma}$ are the cross section and the inelasticity of the process. For the case of the B-H process we employ equation (30) using $\epsilon_0 = \epsilon_{0,\text{BH}}$, $K_{p\gamma} = 2m_e/m_p$, and $\sigma_{p\gamma}$ is taken from Maximon (1968). For the photo-pion interaction we calculate the cooling rate using equation (30) with $\epsilon_0 = \epsilon_{0,\pi}$, and $K_{p\gamma}$, and $\sigma_{p\gamma}$ are obtained following the approach of Atoyan & Dermer (2003).

7 APPENDIX B: PARTICLE EMISSION FLUXES

We derive the MM emission that results from electrons and protons accelerated within the reconnection region in the blazar jet, neglecting the influence of any external radiation field (such as the one produced by the AGN disk, and/or a broad line region). Thus, we consider the Synchrotron radiation of accelerated electrons as the only source of target photons within the emission volume leading to SSC scattering, photo-pion production, Bethe-Heitler pair production, and pair production by photon-photon annihilation. In what

follows, we describe the particle and radiation processes that we account for, with physical quantities defined in the co-moving frame of the emission region, unless we specify quantities in a different frame.

We consider the radiation fields of low and high energy photons as isotropic and uniform within a spherical region of radius r_b and approximate the energy distributions of photon field densities (in $\text{erg}^{-1} \text{cm}^{-3}$) as:

$$n_{\text{ph}}(\epsilon) = \frac{4\pi}{c\epsilon} I_\epsilon. \quad (31)$$

In this equation, I_ϵ is the specific intensity of the radiation field defined as $dE = I_\epsilon dt d\epsilon dA d\Omega$ ($\text{s}^{-1} \text{cm}^{-2} \text{sr}^{-1}$) at a given photon energy ϵ . The simplest solution for I_ϵ in a uniform medium with emission and absorption can be written as:

$$I_\epsilon = j_\epsilon r_b \frac{1 - e^{-\tau}}{\tau}, \quad (32)$$

being j_ϵ the emission coefficient, $\tau \approx r_b \alpha_\epsilon$ the optical depth, and α_ϵ the corresponding absorption coefficient.

7.1 Leptonic emission

Synchrotron photons emitted by accelerated electrons are assumed here as the source of target photons within the emission region as well as the source of the low energy bump in the observed blazar SED. We approximate the photon field density of this Synchrotron emission neglecting the effect of Synchrotron self-absorption:

$$n_{\text{ph}}^{\text{syn}}(\epsilon) = \frac{4\pi j_\epsilon^{\text{syn}} r_b}{c\epsilon}, \quad (33)$$

where j_ϵ^{syn} is the Synchrotron emission coefficient ($\text{s}^{-1} \text{cm}^{-3} \text{sr}^{-1} \text{Hz}^{-1}$) at the photon energy ϵ . Given the energy distribution of primary electrons N'_e (modelled by eq. 16), we obtain the Synchrotron emission coefficient as

$$4\pi j_\epsilon^{\text{syn}} = \int_{E'_e,0}^{\infty} dE''_e N_e(E''_e) \langle P_{\text{syn}}(E''_e) \rangle_\alpha, \quad (34)$$

where $\langle P_{\text{syn}} \rangle_\alpha$ is the angular averaged power of radiation emitted by a single electron of energy E'_e in a random magnetic field, which we calculate using the approach of Aharonian et al. (2010) (their Appendix D). The differential luminosity of Synchrotron photons (luminosity per photon energy) that leaves the emission region is then calculated as:

$$L_\epsilon^{\text{syn}} = V_b 4\pi j_\epsilon^{\text{syn}}, \quad (35)$$

where we approximate the reconnection volume as $V_b = 4\pi r_b^3/3$.

We account for the SSC emission of the accelerated electrons as:

$$L_\epsilon^{\text{SSC}} = V_b 4\pi j_\epsilon^{\text{IC}} [1 - \exp\{-\tau_{\gamma\gamma}(\epsilon)\}] / \tau_{\gamma\gamma}(\epsilon) \quad (36)$$

where j_ϵ^{IC} is the IC emission coefficient, and

$$\tau_{\gamma\gamma}(\epsilon) = r_b \int_{\epsilon_{s,\text{min}}}^{\epsilon_{s,\text{max}}} d\epsilon_s n_{\text{ph}}^{\text{syn}}(\epsilon_s) \sigma_{\gamma\gamma}(\epsilon_s, \epsilon), \quad (37)$$

is the optical depth due to gamma-ray annihilation by pair production within the emission volume. Given the energy distribution of primary electrons N'_e (eq. 16), and the energy density distribution of the target soft photons $n_{\text{ph}}^{\text{syn}}(\epsilon_s)$ (eq. 33), we calculate the IC scattering emission coefficient following the approach of Blumenthal & Gould (1970) which allows for Thompson and Klein-Nishina regimes:

$$4\pi j_\epsilon^{\text{IC}} = \epsilon \int_{E'_{e,0}}^{\infty} dE_e N'_e(E'_e) \int_{\epsilon_{s,0}}^{\epsilon_{s,\text{max}}} d\epsilon_{\text{syn}} n_{\text{ph}}^{\text{syn}}(\epsilon_s) K_{\text{IC}}(\epsilon, \epsilon_s, E'_e),$$

with

$$K_{\text{IC}}(\epsilon, \epsilon_s, E_e) = \frac{3\sigma_{\text{T}}(m_e c^2)^2}{4\epsilon_s E_e^2} F(\epsilon, \epsilon_s, E_e), \quad (38)$$

and $F(\epsilon, \epsilon_s, E_e)$ is given by equation (29). To obtain $\tau_{\gamma\gamma}$ we use the cross section for photon-photon annihilation $\sigma_{\gamma\gamma}$ (see, e.g., Akharian et al. 1985) in the head-on collision limit:

$$\sigma_{\gamma\gamma} = \frac{1}{2} \pi r_e^2 (1 - \beta_0^2) \left[(3 - \beta_0^4) \ln \left\{ \frac{1 + \beta_0}{1 - \beta_0} \right\} + 2\beta_0 (\beta_0^2 - 2) \right], \quad (39)$$

with

$$\beta_0 = \sqrt{1 - \frac{m_e^2 c^4}{\epsilon_s \epsilon}}, \quad (40)$$

where ϵ_s and ϵ are the energies of the low and high energy photons, respectively.

7.2 Hadronic dissipation

In the reconnection region analysed here, we consider proton Synchrotron radiation, photon-pion production, and Bethe-Heitler pair production as the dominant hadronic processes that contribute to observable emission from the blazar flare.

We obtain the differential luminosity due to proton Synchrotron emission similarly as in the case of primary electrons (see eq. 35) but employing the energy distribution of protons derived in eq. (12) as well as the proton mass m_p when evaluating the emission coefficient j_ϵ^{syn} (detailed in section 7.1).

For the photo-pion cooling channel, we account for the injection of particles and photons within the emission region employing the formalism of Kelner & Aharonian (2008) which provides analytical approximations from Monte Carlo simulations performed with the SOPHIA code (Mücke et al. 2000). Given the population of relativistic protons (eq. 12), and the distribution of soft photons (eq. 33), we account for the injection rate q_ℓ ($\text{s}^{-1} \text{erg}^{-3} \text{cm}^{-3}$) of the gamma-rays (γ), neutrinos (ν), anti-neutrinos ($\bar{\nu}$), electrons (e^-), and positrons (e^+) evaluating the expressions:

$$q_\ell(E_\ell) = \int_{\eta_0}^{\infty} d\eta H(\eta, E_\ell),$$

$$H(\eta, E_\ell) = \frac{m_p^2 c^4}{4} \int_{E_\ell}^{\infty} \frac{dE_p}{E_p^2} N_p(E_p) n_{\text{ph}} \left(\frac{\eta m_p^2 c^4}{4E_p} \right) \Phi_\ell \left(\eta, \frac{E_\ell}{E_p} \right), \quad (41)$$

where $\eta_0 = 2 \frac{m_\pi}{m_p} + \frac{m_\pi^2}{m_p^2} \approx 0.313$, the sub-index ℓ labels the products $\ell = \gamma, \nu, \bar{\nu}, e^+, e^-$, and Φ_ℓ is the energy distribution of the type of product ℓ given by equations 27 and 31, and tables I, II and III in Kelner & Aharonian (2008).

Once produced, neutrinos are virtually unimpeded until their potential detection at Earth. We then calculate the differential luminosity of, e.g., muon neutrinos leaving the emission region as:

$$L_{E_\nu} = V_b E_\nu (q_{\nu_\mu} + q_{\bar{\nu}_\mu}), \quad (42)$$

where q_{ν_μ} and $q_{\bar{\nu}_\mu}$ are obtained from eq. 42. The electrons, positrons and gamma-rays injected from the decay of pions in the photo-hadronic channel (see eq. 42), manifest as observable radiation via

electromagnetic cascades within the emission region. We account for such reprocessed radiation as detailed in the next subsection.

When the energy of relativistic protons $E_p = \gamma_p m_p c^2$ and of target soft photons ϵ surpass the threshold $\gamma_p \epsilon > m_e c^2$, we expect direct production of electron-positron pairs by the Bethe-Heitler channel. We account for the injection rate of these pairs ($\text{erg}^{-1} \text{s}^{-1} \text{cm}^{-3}$) in the emission region as:

$$q_e^{\text{B-H}}(E_e) = \int_{E_{p,0}}^{\infty} dE_p N_p(E_p) \Phi_{\text{BH}}(E_p, E_e), \quad (44)$$

where

$$\begin{aligned} \Phi_{\text{BH}}(E_p, E_e) = & \frac{1}{2\gamma_p^3 m_e c} \int_{\frac{(\gamma_p + \gamma_e)^2}{4\gamma_p^2 \gamma_e}}^{\infty} d\tilde{\epsilon} \frac{\tilde{n}(\tilde{\epsilon})}{\tilde{\epsilon}^2} \\ & \times \int_{\frac{(\gamma_p + \gamma_e)^2}{2\gamma_p \gamma_e}}^{2\gamma_p \tilde{\epsilon}} d\omega \int_{\frac{\gamma_p^2 + \gamma_e^2}{2\gamma_p \gamma_e}}^{\omega-1} d\tilde{\gamma}_- \frac{W(\omega, \tilde{\gamma}_-, \xi)}{\tilde{p}_-}, \end{aligned} \quad (45)$$

is the injection rate of electrons by a proton of energy E_p as presented in [Kelner & Aharonian \(2008\)](#), with W being the differential cross section of the process in the rest frame of the proton taken from [Blumenthal \(1970\)](#). In eq. (45), $\gamma_{e,p} = \frac{E_{e,p}}{m_e c^2}$ are the Lorentz factor of the electrons and protons in the emission volume frame, $\tilde{\epsilon} = \frac{\epsilon}{m_e c^2}$ and $\tilde{n} = m_e c^2 n_{\text{ph}}$ are the normalised energy and differential energy density of the target photons (see equation 33), $\tilde{\gamma}_- = \frac{E_-}{m_e c^2}$ is the Lorentz factor of the produced electrons in the rest frame of the relativistic proton, $\tilde{p}_- = \sqrt{\tilde{\gamma}_-^2 - 1}$ is the momentum modulus of these electrons normalised by $m_e c$, and $\xi = (\gamma_p \tilde{\gamma}_- - \gamma_e) / (\gamma_p \tilde{p}_-)$.

7.3 Emission from hadronic cascades

In the present emission model, we account for electromagnetic cascades initiated by electrons, positrons, and gamma-rays from the photo-pion channel, as well as from electron-positron pairs from the Bethe-Heitler process. Such cascades proceed by the radiative cooling of secondary electrons and positrons whose radiation can be highly energetic to annihilate from the interaction with the soft-photon fields within the emission region. The photon-photon annihilation creates further electron-positron pairs which cool by radiation and so on.

Given the number density ($\text{erg}^{-1} \text{cm}^{-3}$) of the high and soft photon fields n^{h} and n^{soft} , respectively, we compute the injection rate $q_{ee}^{\gamma\gamma}$ of electron-positron pairs ($\text{erg}^{-1} \text{s}^{-1} \text{cm}^{-3}$) due to photon-photon annihilation following the approach of [Agaronyan et al. \(1983\)](#):

$$\begin{aligned} q_{ee}^{\gamma\gamma}(E_e) = & 2 \frac{3}{32} \frac{c\sigma_T}{m_e c^2} \int_{\gamma_e}^{\infty} d\xi_1 \frac{\tilde{n}_1(\xi_1)}{\xi_1^3} \int_{\frac{\xi_1}{4\gamma_e(\xi_1 - \gamma_e)}}^{\infty} d\xi_2 \frac{\tilde{n}_2(\xi_2)}{\xi_2^2} \\ & \times \left[\frac{4\xi_1^2}{\gamma_e(\xi_1 - \gamma_e)} \ln \left\{ \frac{4\xi_2 \gamma_e(\xi_1 - \gamma_e)}{\xi_1} \right\} - 8\xi_1 \xi_2 \right. \\ & \left. + \frac{2(2\xi_1 \xi_2 - 1)\xi_1^2}{\gamma_e(\xi_1 - \gamma_e)} - \left(1 - \frac{1}{\xi_1 \xi_2} \right) \frac{\xi_1^4}{\gamma_e^2(\xi_1 - \gamma_e)^2} \right], \end{aligned} \quad (46)$$

where $\gamma_e = E_e / (m_e c^2)$, $\tilde{n}_2 = m_e c^2 n^{\text{soft}}$, $\tilde{n}_1 = m_e c^2 n^{\text{h}}$, and $\xi_1 = \epsilon_1 / (m_e c^2)$ and $\xi_2 = \epsilon_2 / (m_e c^2)$ are the high and low energy photons, respectively, normalised by the electron rest mass energy. This approach to obtain the pair injection is valid when $\epsilon_2 \ll m_e c^2 \leq \epsilon_1$, which is the case of the blazar emission model discussed in this paper.

We use eqs. (31-32) to compute the high energy photon-field employing the specific intensity:

$$I_\epsilon^{\text{h}} = r_{\text{rec}} j_\epsilon^{\text{h}} [1 - \exp\{-\tau_{\gamma\gamma}(\epsilon)\}] / \tau_{\gamma\gamma}(\epsilon) \quad (47)$$

where j_ϵ^{h} is the emission coefficient of the high energy photons and $\tau_{\gamma\gamma}$ their optical depth to gamma-ray absorption (given by eq. 37). In all cases, we employ the photon distribution given by eq. 33 as the low energy photon field density.

To calculate the emission of the injected electron/positrons from photon-photon annihilations, the decay of charged pions, and the Bethe-Heitler process, we consider the electron energy distribution N_e ($\text{erg}^{-1} \text{cm}^{-3}$) as the stationary solution of the particle transport equation ([Ginzburg & Syrovatskii 1964](#); [Romero et al. 2010](#)):

$$N_e(E_e) = \frac{\int_{E_e}^{\infty} dE'_e q_{e,\text{inj}}(E'_e) \exp\left\{-\int_{E_e}^{E'_e} \frac{dE''_e}{|P_e(E''_e) t_{\text{esc}}(E''_e)|}\right\}}{|P_e(E_e)|}. \quad (48)$$

In this equation, $q_{e,\text{inj}}$ is the corresponding electron injection rate (given by eqs. 42, 44, or 46), P_e the power of their radiative cooling, and t_{esc} is the electron escaping time which can be considered as the minimum among the advection and diffusion time scales. In this work, we perform our calculations neglecting the argument of the exponential function in the solution given by eq. 48, which is a valid assumption as long as t_{adv} and t_{diff} are much longer than the electron cooling time scales. We find that secondary electrons/positrons (which are in general more energetic than primary electrons) have indeed cooling times negligible when compared to the corresponding advection time for the radiation solutions derived in this paper. The emission spectrum produced by these secondary electron and positrons is then computed as

$$L_\epsilon^{\text{syn},e\pm} = V_b 4\pi j_\epsilon^{\text{syn}} [1 - \exp\{-\tau_{\gamma\gamma}(\epsilon)\}] / \tau_{\gamma\gamma}(\epsilon), \quad (49)$$

where $\tau_{\gamma\gamma}$ is given by eq. (37) and j_ϵ^{syn} is given by eq. (34).

In our emission model, we account for the contribution to the blazar spectrum of EM cascades triggered by neutral pion (π^0) decay, charge pion (π^\pm) decay, and B-H pair production, as stressed. The cascade from the π^0 channel initiates with the injection of gamma-rays for which we employ eq. 47 using the emission coefficient $j_\epsilon^{\text{h}} = \frac{\epsilon}{4\pi} q_\gamma$ and q_γ obtained from eq. 42. The cascade from the π^\pm channel initiates with the injection of electrons and positrons for which we employ eq. 48, using the electron injection rate $q_{e,\text{inj}} = q_{e+} + q_{e-}$ (with q_{e+} and q_{e-} given by eq. 42). The cascade from the B-H channel initiates with the injection of electron-positron pairs, and in this case we apply eq. (48), with $q_{e,\text{inj}} = q_{e\pm}^{\text{B-H}}$ from eq. 44).

7.4 Observed fluxes

Our emission model assumes the trajectory of the emitting blob as quasi-aligned to the line of sight with an angle $\theta_b < 1/\Gamma_j$. Under this condition, we calculate the observed flux ($\text{erg s}^{-1} \text{cm}^{-2}$) of an emission component at the observed energy E , as

$$EF_E = \frac{\Gamma_j^4 \epsilon L_\epsilon}{4\pi D_L^2} \exp\{-\tau_{\gamma\gamma}^{\text{eg}}(E, z)\}, \quad (50)$$

where ϵ and $E = \epsilon\Gamma_j/(1+z)$ are the emission energies at the source and the observer frames, respectively, z and D_L are the redshift and luminosity distance of the source, respectively, and L_ϵ is the differential luminosity of the emission component in the source frame (see eqs. 35, 36, 43, and 49). We assume the source with a redshift and luminosity distance of $z = 0.34$ and $D_L = 1750$ Mpc, respectively ([IceCube Collaboration et al. 2018b](#)). The attenuation of the blazar

emission due to the extragalactic light (EBL) is accounted by the attenuation coefficient in the exponential factor in the RHS of eq. 50, which is relevant for the emission components producing photons at GeV-TeV energies. We calculate this coefficient using the gammapy package (Donath et al. 2023), adopting the EBL absorption model of Domínguez et al. (2011)

REFERENCES

- Abbasi R., et al., 2022, *ApJ*, **938**, 38
- Ackermann M., et al., 2016, *ApJ*, **824**, L20
- Agaronyan F. A., Atayan A. M., Nagapetyan A. M., 1983, *Astrophysics*, **19**, 187
- Aharonian F., et al., 2007, *ApJ*, **664**, L71
- Aharonian F. A., Kelner S. R., Prosekin A. Y., 2010, *Phys. Rev. D*, **82**, 043002
- Akharonian F. A., Kririllov-Ugrumov V. G., Vardanian V. V., 1985, *Ap&SS*, **115**, 201
- Ansoldi S., et al., 2018, *ApJ*, **863**, L10
- Atayan A. M., Dermer C. D., 2003, *ApJ*, **586**, 79
- Bellenghi C., Padovani P., Resconi E., Giommi P., 2023, *ApJ*, **955**, L32
- Beresnyak A., Li H., 2016, *ApJ*, **819**, 90
- Blandford R. D., Znajek R. L., 1977, *MNRAS*, **179**, 433
- Blumenthal G. R., 1970, *Phys. Rev. D*, **1**, 1596
- Blumenthal G. R., Gould R. J., 1970, *Reviews of Modern Physics*, **42**, 237
- Britto R. J., Bottacini E., Lott B., Razaque S., Buson S., 2016, *ApJ*, **830**, 162
- Buson S., Tramacere A., Pfeiffer L., Oswald L., de Menezes R., Azzollini A., Ajello M., 2022, *ApJ*, **933**, L43
- Cerruti M., 2020, in *Journal of Physics Conference Series*. p. 012094 ([arXiv:1912.03666](https://arxiv.org/abs/1912.03666)), doi:10.1088/1742-6596/1468/1/012094
- Cerruti M., Zech A., Boisson C., Emery G., Inoue S., Lenain J. P., 2019, *MNRAS*, **483**, L12
- Comisso L., Sironi L., 2018, *Phys. Rev. Lett.*, **121**, 255101
- Davelaar J., Philippov A. A., Bromberg O., Singh C. B., 2020, *ApJ*, **896**, L31
- Domínguez A., et al., 2011, *MNRAS*, **410**, 2556
- Donath A., et al., 2023, *A&A*, **678**, A157
- Gao S., Fedynitch A., Winter W., Pohl M., 2019, *Nature Astronomy*, **3**, 88
- García-Morillo M., Alexakis Alexandros J., 2024, *arXiv e-prints*, p. [arXiv:2406.08951](https://arxiv.org/abs/2406.08951)
- Ghisellini G., 2013, *Radiative Processes in High Energy Astrophysics. Lecture Notes in Physics Vol. 873*, Springer, Berlin, Germany, doi:10.1007/978-3-319-00612-3
- Giannios D., 2010, *MNRAS*, **408**, L46
- Giannios D., Uzdensky D. A., 2019, *MNRAS*, **484**, 1378
- Giannios D., Uzdensky D. A., Begelman M. C., 2009, *MNRAS*, **395**, L29
- Ginzburg V. L., Syrovatskii S. I., 1964, *The Origin of Cosmic Rays*
- Guo F., Li X., Daughton W., Kilian P., Li H., Liu Y.-H., Yan W., Ma D., 2019, *ApJ*, **879**, L23
- Guo F., Liu Y.-H., Li X., Li H., Daughton W., Kilian P., 2020, *Physics of Plasmas*, **27**, 080501
- Guo F., et al., 2022, *arXiv e-prints*, p. [arXiv:2208.03435](https://arxiv.org/abs/2208.03435)
- Hovatta T., Lindfors E., 2019, *New Astron. Rev.*, **87**, 101541
- Hovatta T., Valtaoja E., Tornikoski M., Lähteenmäki A., 2009, *A&A*, **494**, 527
- Hovatta T., et al., 2021, *A&A*, **650**, A83
- Hussain S., Alves Batista R., de Gouveia Dal Pino E. M., Dolag K., 2023, *Nature Communications*, **14**, 2486
- Hussain S., de Gouveia Dal Pino E. M., Pagliaroli G., 2024, *ApJ*, **960**, 124
- IceCube Collaboration et al., 2018a, *Science*, **361**, 147
- IceCube Collaboration et al., 2018b, *Science*, **361**, eaat1378
- Kadowaki L. H. S., de Gouveia Dal Pino E. M., Stone J. M., 2018, *The Astrophysical Journal*, **864**, 52
- Kadowaki L. H. S., de Gouveia Dal Pino E. M., Medina-Torrejón T. E., Mizuno Y., Kushwaha P., 2021, *ApJ*, **912**, 109
- Keivani A., et al., 2018, *ApJ*, **864**, 84
- Kelner S. R., Aharonian F. A., 2008, *Phys. Rev. D*, **78**, 034013
- Khiali B., de Gouveia Dal Pino E. M., 2016, *MNRAS*, **455**, 838
- Khiali B., de Gouveia Dal Pino E. M., del Valle M. V., 2015, *MNRAS*, **449**, 34
- Kilian P., Li X., Guo F., Li H., 2020, *ApJ*, **899**, 151
- Kowal G., Lazarian A., Vishniac E. T., Otmianowska-Mazur K., 2009, *ApJ*, **700**, 63
- Kowal G., de Gouveia Dal Pino E. M., Lazarian A., 2011, *ApJ*, **735**, 102
- Kowal G., de Gouveia Dal Pino E. M., Lazarian A., 2012, *Phys. Rev. Lett.*, **108**, 241102
- Kowal G., Falceta-Gonçalves D. A., Lazarian A., Vishniac E. T., 2020, *ApJ*, **892**, 50
- Lazarian A., Vishniac E. T., 1999, *ApJ*, **517**, 700
- Li X., Guo F., Li H., Li G., 2015, *ApJ*, **811**, L24
- Liodakis I., Petropoulou M., 2020, *ApJ*, **893**, L20
- Lister M. L., et al., 2019, *ApJ*, **874**, 43
- Liu Y.-H., Hesse M., Guo F., Daughton W., Li H., Cassak P. A., Shay M. A., 2017, *Phys. Rev. Lett.*, **118**, 085101
- Liu R.-Y., Wang K., Xue R., Taylor A. M., Wang X.-Y., Li Z., Yan H., 2019, *Phys. Rev. D*, **99**, 063008
- Longair M. S., 2011, *High Energy Astrophysics*
- Lyubarsky Y., Liverts M., 2008, *ApJ*, **682**, 1436
- Lyutikov M., Sironi L., Komissarov S. S., Porth O., 2017, *Journal of Plasma Physics*, **83**, 635830602
- Maximon L. C., 1968, *J. Res. Nat. Bur. Stand.*,
- McKinney J. C., Tchekhovskoy A., Blandford R. D., 2012, *MNRAS*, **423**, 3083
- Medina-Torrejón T. E., de Gouveia Dal Pino E. M., Kadowaki L. H. S., Kowal G., Singh C. B., Mizuno Y., 2021, *ApJ*, **908**, 193
- Medina-Torrejón T. E., de Gouveia Dal Pino E. M., Kowal G., 2023, *ApJ*, **952**, 168
- Mücke A., Engel R., Rachen J. P., Protheroe R. J., Stanev T., 2000, *Computer Physics Communications*, **124**, 290
- Nishikawa K., et al., 2020, *MNRAS*, **493**, 2652
- Padovani P., Oikonomou F., Petropoulou M., Giommi P., Resconi E., 2019, *MNRAS*, **484**, L104
- Paiano S., Falomo R., Treves A., Scarpa R., 2018, *ApJ*, **854**, L32
- Petropoulou M., Giannios D., Sironi L., 2016, *MNRAS*, **462**, 3325
- Plavin A., Kovalev Y. Y., Kovalev Y. A., Troitsky S., 2020, *ApJ*, **894**, 101
- Plavin A. V., Kovalev Y. Y., Kovalev Y. A., Troitsky S. V., 2021, *ApJ*, **908**, 157
- Rees M. J., 1966, *Nature*, **211**, 468
- Ripperda B., Porth O., Xia C., Keppens R., 2017, *MNRAS*, **471**, 3465
- Rodríguez-Ramírez J. C., de Gouveia Dal Pino E. M., Alves Batista R., 2019, *ApJ*, **879**, 6
- Romero G. E., Vieyro F. L., Vila G. S., 2010, *A&A*, **519**, A109
- Sahakyan N., 2018, *ApJ*, **866**, 109
- Singh C. B., Mizuno Y., de Gouveia Dal Pino E. M., 2016, *ApJ*, **824**, 48
- Sironi L., Spitkovsky A., 2014, *ApJ*, **783**, L21
- Takamoto M., Inoue T., Lazarian A., 2015, *ApJ*, **815**, 16
- Vicentin G. H., Kowal G., de Gouveia Dal Pino E. M., Lazarian A., 2024, *arXiv e-prints*, p. [arXiv:2405.15909](https://arxiv.org/abs/2405.15909)
- Werner G. R., Philippov A. A., Uzdensky D. A., 2019, *MNRAS*, **482**, L60
- Xu S., Lazarian A., 2023, *ApJ*, **942**, 21
- Xue R., Liu R.-Y., Petropoulou M., Oikonomou F., Wang Z.-R., Wang K., Wang X.-Y., 2019, *ApJ*, **886**, 23
- Zdziarski A. A., Bottcher M., 2015, *MNRAS*, **450**, L21
- Zhang J.-F., Xu S., Lazarian A., Kowal G., 2023a, *Journal of High Energy Astrophysics*, **40**, 1
- Zhang H., Sironi L., Giannios D., Petropoulou M., 2023b, *ApJ*, **956**, L36
- de Gouveia Dal Pino E. M., Kowal G., 2015, *Particle Acceleration by Magnetic Reconnection*. Springer Berlin Heidelberg, p. 373, doi:10.1007/978-3-662-44625-6_13
- de Gouveia Dal Pino E. M., Lazarian A., 2005, *A&A*, **441**, 845
- de Gouveia Dal Pino E. M., Medina-Torrejón T. E., 2024, *arXiv e-prints*, p. [arXiv:2410.13071](https://arxiv.org/abs/2410.13071)
- de Gouveia Dal Pino E. M., Kowal G., Kadowaki L., Medina-Torrejón T. E., Mizuno Y., Singh C., 2020, in Asada K., de Gouveia Dal Pino E., Giro-

letti M., Nagai H., Nemmen R., eds, IAU Symposium Vol. 342, IAU Symposium. pp 13–18, doi:[10.1017/S1743921318007688](https://doi.org/10.1017/S1743921318007688)
de Gouveia dal Pino E. M., Opher R., 1991, A&A, [242](#), [319](#)
del Valle M. V., de Gouveia Dal Pino E. M., Kowal G., 2016, MNRAS, [463](#),
[4331](#)

This paper has been typeset from a \TeX/L\AA\TeX file prepared by the author.